

Boosting structural stability of lead-free Tin-based layered double perovskite nanocrystals with enhanced photoelectrochemical activity

Downloaded from: https://research.chalmers.se, 2026-11-25 08:04 UTC

Citation for the original published paper (version of record):
Rahman, S., Ngoipala, A., Yukta et al (2026). Boosting structural stability of lead-free Tin-based layered double perovskite nanocrystals
with enhanced photoelectrochemical activity. Communications Materials, 7(1).
http://dx.doi.org/10.1038/s43246-026-01388-3

N.B. When citing this work, cite the original published paper.

research.chalmers.se offers the possibility of retrieving research publications produced at Chalmers University of Technology. It covers all kind of research output: articles, dissertations, conference papers, reports etc. since 2004. research.chalmers.se is administrated and maintained by Chalmers Library

(article starts on next page)

communications materials

A Nature Portfolio journal

Article

https://doi.org/10.1038/s43246-026-01388-3

Boosting structural stability of lead-free Tin-based layered double perovskite nanocrystals with enhanced photoelectrochemical activity

Check for updates

Sunardi Rahman[1,2,3], Apinya Ngoipala[4], Yukta[1,2,3], Qi Shi[3,5], Archit Dhingra[6], Tianyi Hu[1,2,3], Vipinraj Sugathan[1,3], Sara Blidberg[1], Klara Palmqvist[1], Tarek Al Said[7], Sri Kasi Matta[8], Qinqi Zhou[1,2,3], Jiatu Liu[9], Weimin Wang[6], Kimberly A. Dick[1,2,3], Tönu Pullerits[3,5], Julia Wiktor[4] & Maning Liu[1,2,3] ✉

Recently, a new family of quasi-2D lead-free layered double perovskites in a formula $Cs_4M(II)M(III)_2Cl_{12}$ has attracted increasing attention, particularly in the form of colloidal nanocrystals (NCs). Herein, we successfully coordinate Sn(II) at M(II) site in this layered structure while tailoring M(III) site with two types of trivalent cations, eventually forming $Cs_4SnIn_2Cl_{12}$ (CTIC) and $Cs_4SnSb_2Cl_{12}$ (CTAC) NCs. We observe the formation of a self-trapped excited state in both cases. CTIC exhibits bright transition with a relatively high photoluminescence quantum yield of 12%. Both NCs are employed as photoanodes to construct a photoelectrochemical (PEC) cell for realizing a redox reaction with benzoquinone as the intermediate reactant. CTAC achieves the highest photocurrent density (60 μA cm^{-2}) under 1 Sun condition, which is amongst the highest for lead-free perovskite PEC reactions. More importantly, the Sn(II) cation state of CTIC NCs can be maintained even after 300 days of air storage, highlighting the effectiveness of this new quasi-2D layered structure on stabilizing Sn(II) perovskites.

Tin (Sn)-based halide perovskite nanocrystals (PNCs), namely $ASnX_3$ (A = Cs^+, MA^+; X = Cl^-, Br^- and I^-), have drawn extensive attention as one promising alternative to their highly toxic lead (Pb)-based counterparts, due to lower toxicity, wide range of tunable bandgap (down to 1.3 eV for $MASnI_3$), and pronounced quantum confinement effect for diverse applications such as solar cells, light-emitting diodes (LEDs) and recent photoelectrochemical (PEC) catalysis[1–4]. Moreover, its relatively strong spin-orbit coupling of ~0.43 eV, which is comparable or even higher than that of Pb-based ones, further enhances the suitability for spintronic applications[5,6]. On the other hand, the rapid oxidation of Sn^{2+} into Sn^{4+} under ambient conditions is, in turn, a big barrier for developing stable $ASnX_3$ perovskites, as it leads to the inherently high density of surface defects, e.g., Sn(II) vacancies and shallow trap states[7,8]. To mitigate the structural stability issue, Sn^{4+} oxidation state is directly investigated as a vacancy-ordered double perovskites in a formula of $Cs_2Sn[V]X_6$, in which an isolated $[SnX_6]^{2-}$ vacancy site separates octahedra. This isolated octahedral configuration leads to intrinsic defect tolerance, which is favorable for charge carrier dynamics[9]. For instance, this photophysical picture can be seen of the Cs_2SnX_6 nanocrystals through tunable emission ranging from 444 nm for Cs_2SnCl_6 to 790 nm for Cs_2SnI_6[10,11]. These interesting photophysical properties show long-lived and stable mobile carriers stemming from intrinsic defect tolerance, which can be translated directly as promising photoelectrochemical and photocatalytic applications. Specifically, Cs_2SnI_6 has already exhibited a direct photocurrent density of ~3 μA cm^{-2} by combining charge carrier dynamics and theoretical studies; in this space, anchoring Pt-I_3 on the perovskite can enhance charge separation, which increases the photocurrent density to ~11 μA cm^{-2}[12]. Furthermore, Li's group reported that Cs_2SnBr_6 exhibits a photocurrent density of ~2 μA cm^{-2}, and then, via doping with Pt, this increases significantly to ~15 μA cm^{-2}[9]. Although these materials exhibit better stability than the pristine Sn(II) perovskites, their photocurrent

[1]Centre for Analysis and Synthesis, Department of Chemistry, Lund University, Lund 221 00, P.O. Box 124, Sweden. [2]Wallenberg Initiative Materials Science for Sustainability, Department of Chemistry, Lund University, Lund 221 00, Sweden. [3]NanoLund, Lund University, Professorsgatan 1, Lund 223 63, Sweden. [4]Department of Physics and Astronomy, Chalmers University of Technology, Gothenburg, SE-412 96, Sweden. [5]Chemical Physics, Department of Chemistry, Lund University, Kemicentrum Naturvetarevägen 16, Lund 223 62, Sweden. [6]FinEstBeAMS, MAX IV Laboratory, Fotongatan 2, Lund, Lund 224 84, Sweden. [7]Helmholtz-Zentrum Berlin für Materialien und Energie, Hahn-Meitner-Platz 1, Berlin 14109, Germany. [8]The Queensland University of Technology, Brisbane, QLD 4000, Australia. [9]Deutsches Elektronen-Synchrotron DESY, Hamburg D-22607, Germany. ✉e-mail: maning.liu@chem.lu.se

densities and charge separation remain relatively low due to the possible presence of Sn^{4+} impeding the electronic charge behavior. Therefore, Sn^{2+} is still a preferable valence state in perovskite to improve electronic charge and photophysical properties, but with more effort required in significantly improving their structural stability particularly in ambient conditions.

Recently, a new subclass of quasi-2D lead-free perovskites, namely vacancy-ordered layered double perovskites (LDP) with formula $A_4M(II)M(III)_2X_{12}$ (M(II) is a divalent cation), has been successfully synthesized, particularly in the form of nanocrystals[13]. Compared to the conventional 3D double perovskites, these LDPs feature a direct bandgap nature and adopt a layered structure in which the unit cell typically consists of a single $[M(II)X_6]^{4-}$ octahedron layer sandwiched between two adjacent $[M(III)X_6]^{3-}$ octahedron layers[14]. This structural characteristic endows them to possess several attractive merits, such as a wide range of tunable bandgaps (ca. 1.0–3.8 eV), robust structural stability, large compositional space, and relatively small carrier effective mass. Chen's group first synthesized colloidal Sb-based LDP nanocrystals (LDPNCs) via the hot-injection method, i.e., $Cs_4CuSb_2Cl_{12}$, demonstrating sustained optical performance for up to two months and thermal stability up to 125 °C[15]. Following Chen's work, Caruso's group continued to synthesize $Cs_4ZnSb_2Cl_{12}$ LDPNCs and carried out the photostability test by exposing the materials to continuous 1 Sun illumination. Their test exhibits preserved structural stability up to 1 week, while the LDPNCs are stable in a solvent with a low dielectric constant (<25)[16]. In addition to the stability studies, these groups also show that the LDPNCs can be employed as effective light absorbers for the applications of ultrafast photodetector and photocatalytic toluene oxidation. However, the room-temperature photoluminescence (PL) was hardly observed in these studies, mainly due to the dark (nonradiative) transition of as-formed self-trapped excitons (STEs), which are intrinsically photogenerated in this class of LDP structures[17]. To this end, Liu's group investigated the photophysical behavior of the LDP structure through lattice engineering with substituted trivalent cations of In^{3+} and Bi^{3+} at M(III) site, as well as diverse combinations with transition metal ions at M(II) site such as Co^{2+}, Cu^{2+}, and Zn^{2+}, eventually achieving a highest PL quantum yield (PLQY) of 11.3% with the case of $Cs_4ZnIn_2Cl_{12}$ nanocrystals[17–19]. This series of works has signified the importance of both M(II) and M(III) sites engineering in driving the light (radiative) transition of STEs in LDPNCs. Additionally, nearly all reported LDPNCs exhibit excellent structural and air stability, attributed to the protective outer $[M(III)X_6]$ octahedron layers, which shield the central $[M(II)X_6]$ octahedron layer within the unit cell and effectively hinder the penetration of moisture and oxygen into the perovskite lattice. More interestingly, this type of lead-free LDPNCs is highly suitable for the photocatalytic or even photoelectrochemical (PEC) reactions, ascribed to their good colloidal stability in nonaqueous electrolytes and characteristic layered structure for enlarging the active photocatalytic area. For instance, $Cs_4CuSb_2Cl_{12}$ demonstrates rapid photoresponse along with a steady photocurrent density of ~6 μA cm^{-2}[20]. Also, $Cs_4CoBi_2Cl_{12}$ exhibits the highest photocurrent density of ≈150 μA cm^{-2} at 1.6 V and ≈ 40 μA cm^{-2} at 1.03 V in the suitable oxygen evolution reaction (OER) application[19]. Collectively, these aforementioned studies have motivated us to incorporate air-sensitive Sn(II) cations as the middle octahedron layer within the LDP framework, thereby simultaneously leveraging the inherent structural stability of the LDP architecture. Moreover, early theoretical studies have also predicted the favorable thermodynamic stability of Sn(II)-based LDPs[21]. However, to the best of our knowledge, there has been no experimental evidence for the formation of Sn(II)-based LDPs in any form of crystals.

In this work, we have successfully synthesized the colloidal $Cs_4Sn(II)M(III)_2Cl_{12}$ LDPNCs by tuning the M(III) site into two cases, i.e., $Cs_4SnIn_2Cl_{12}$ and $Cs_4SnSb_2Cl_{12}$, with a wide tunable range of direct band gaps of 3.77 and 2.64 eV, respectively. A relatively strong green emission (529 nm) with a PLQY of ~12% has been observed only from the $Cs_4SnIn_2Cl_{12}$ PNCs, which was absent in the case of $Cs_4SnSb_2Cl_{12}$ PNCs, reflecting different excited-state relaxation pathways in the two materials. Moreover, both PNCs have been utilized as the photoanode for realizing effective PEC reactions with organic compound benzoquinone as the redox intermedium, leading to the generation of a relatively high photocurrent density of ~ 60 μA/cm^2 at 1.03 $V_{Ag/AgCl}$ by the $Cs_4SnSb_2Cl_{12}$ PNCs, mainly attributed to the enhanced light harvesting and swift charge carrier mobility. Moreover, the $Cs_4SnIn_2Cl_{12}$ PNCs demonstrate extremely high structural stability by retaining the Sn(II) cation state even after 300 days of storage in ambient conditions. This remarkable stability can be attributed to two prominent factors: (i) the intrinsic LDP architecture, in which inserted $[SnCl_6]$ octahedron is encapsulated between two adjacent $[InCl_6]$ octahedral layers, providing effective bulky protection; (ii) the formation of an ultrathin (<3 nm) In_2O_3 layer on the surface, which further suppresses the oxidation of Sn(II) to Sn(IV) states. Our work provides a significant pathway for effectively improving the performance and stability of Sn(II)-based perovskites, particularly for future PEC applications.

Results

Crystal structure and morphology of CTIC and CTAC PNCs

Colloidal Sn(II)-based LDPNCs, namely $Cs_4SnIn_2Cl_{12}$ (denoted as CTIC) and $Cs_4SnSb_2Cl_{12}$ (denoted as CTAC), were successfully synthesized via a modified hot-injection method for initiating a rapid nucleation process upon the swift injection of a separate chlorine precursor (i.e., chlorotrimethylsilane, TMS-Cl) into a mixed metal ion-ligand precursor[17–19]. The synthesis details are described in the Method section. It is noted that the optimized injection temperature (230 °C) to form CTAC NCs is higher than that (180 °C) of CTIC NCs, which has been observed previously for other types of Sb-based LDPNCs[19]. This is plausibly due to the stronger Sb-Cl and Sb-ligand bonding in the CTAC precursor compared to the In-Cl and In-ligand bonding in the CTIC precursor, requiring higher activation energy and consequently higher thermal energy for swift nucleation and growth[22]. The nominal LDP structure of Sn(II)-based PNCs in a unit cell is presented in Fig. 1a, highlighting the coordination of $[SnCl_6]^{4-}$ octahedron as the inserted layer. The X-ray diffraction (XRD) patterns of as-synthesized Sn-based NCs in powder form are shown in Fig. 1b, by comparing with the recently reported Cu(II)-based LDPNCs, i.e., $Cs_4CuSb_2Cl_{12}$, as the reference (ICSD 243918)[15]. The structural match was also performed via Rietveld refinement, as shown in Fig. S1 and Table S1 in the supporting information (SI). Both CTIC and CTAC PNCs demonstrate the identical family of this LDP structure with a space group C2/m, following a few major characteristic peaks approximately at 24° and 25° (assigned to $(\bar{3}11)$ and (020), 28° and 29° (assigned to (022) and (400)), and 33.4° and 34.8° (assigned to; $(40\bar{4})$ and $(2\bar{2}2)$), respectively[15]. Interestingly, the XRD pattern of CTIC PNCs demonstrates a few single broad peaks that stem from the merging of corresponding dual characteristic peaks, such as (020), (400), and $(2\bar{2}2)$. This may suggest that the interaction between the oleic acid (OA^-) ligand and the surface of CTIC PNCs is stronger than that of CTAC PNCs. In the former case, the stronger ligand-surface interaction can confine the oriented growth, resulting in relatively lower crystallinity[16]. As observed in the XRD pattern of CTAC PNCs, the metathesis reaction at higher temperature (ca. 230 °C) yields a larger nanocrystal size with a more pronounced dual-peak feature, indicative of a lower adsorption energy of the OA ligand that is capped to the surface of PNCs, which will be confirmed upon the infrared (IR) spectra in the following section. It is further noted that two peaks at $(\bar{3}11)$ and (020) in the pattern of CTAC shift to lower Bragg angles compared to the reference Cu/Sb-based pattern, revealing that an internal expansion may occur in the lattice of M(II) site as their M(III) site is identical (i.e., Sb^{3+}). This is possibly ascribed to a larger ionic radius (115 pm) of Sn^{2+}, relative to that (73 pm) of Cu^{2+}. On the other hand, CTIC pattern peaks shift back to reference, possibly due to the larger ionic radius of In^{3+} (80 pm) compared to Sb^{3+} (76 pm) for the lattice offset effect [23].

Furthermore, the morphology of as-synthesized LDPNCs was confirmed upon the transmission electron microscopy (TEM) measurements, as presented in Fig. 1c (for CTIC) and 1 f (for CTAC), respectively. A clear hexagonal shape has been observed for CTIC PNCs with an average nanocrystal size of 41.4 ± 2.3 nm. However, some subtle aggregation has been repeatedly detected in the case of CTAC PNCs even with quite fresh sample preparation. The irregularity of CTAC PNCs with cluster-like

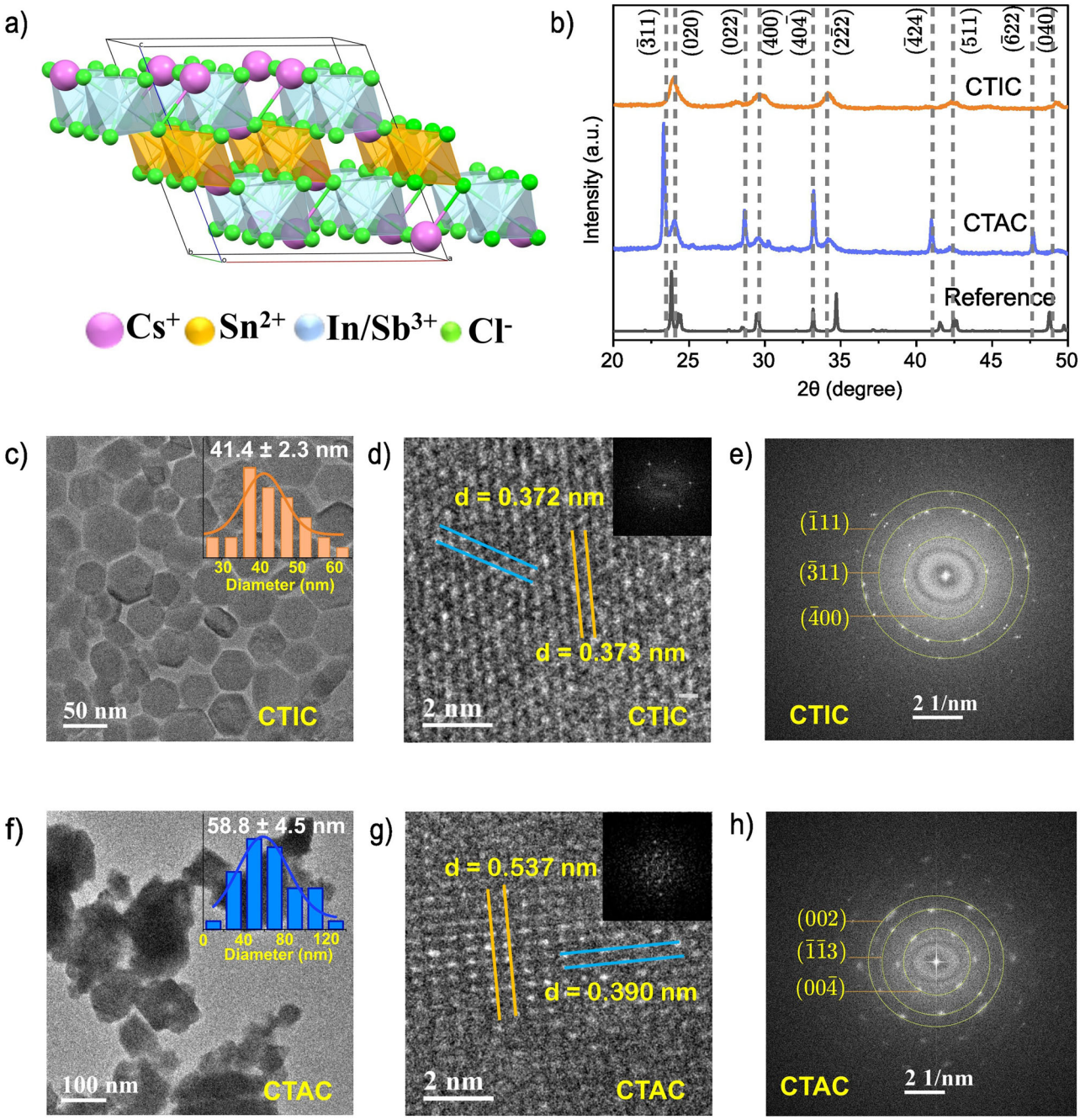

Fig. 1 | Structural analysis and morphology. a Unit cell layout of nominal layered double perovskite structure for LDPNCs. **b** XRD patterns of as-synthesized LDPNCs. The dash lines highlight the characteristic peaks, compared with the reference pattern of the $Cs_4CuSb_2Cl_{12}$ single crystal. **c**, **f** TEM images with size distribution histograms of CTIC and CTAC PNCs, respectively. **d**, **g** HR-TEM images with *d*-spacing and FFT of SAED pattern. **e**, **h** FFT patterns of polycrystalline LDPNCs.

morphology exhibits a larger average nanocrystal size of 58.8 ± 4.5 nm compared to the CTIC case, which is in good agreement with previous XRD analysis. The dynamic movement of the ligands, i.e., OA^- and oleylamine (OAm^+) at high temperature (e.g., 230 °C for CTAC), may weaken the control over ligand-monomer attachment and detachment process that initially form the clusters[16]. This growth environment can consequently promote the formation of aggregated nanocrystals[6,16], similarly observed for other reported Sb-based PNCs such as $Cs_4CoSb_2Cl_{12}$ and $Cs_3Sb_2Cl_9$ with a high metathesis reaction temperature[19,24]. Our high-resolution TEM (HR-TEM) images (see Fig. 1d, g) display a well-defined LDP structure in both PNCs cases with the fast Fourier transform (FFT) images selected area electron diffraction (SAED) patterns (inset images). The lattice fringes of CTAC PNCs generally show longer *d*-spacing distances in diverse planes, such as 0.390 nm for CTAC and 0.372 nm for CTIC, suggesting that the M(III) site (i.e., In or Sb) could initiate a distinct interlayer stacking in the LDP structure as well as a variable degree of octahedral tilting with adjacent [$SnCl_6$] octahedron. The FFT pattern of polycrystalline CTIC (Fig. 1e, h) demonstrates indexing ($\bar{1}11$), ($\bar{3}11$), and ($\bar{4}00$), while CTAC exhibit those of (002), ($\bar{1}\bar{1}3$), and ($00\bar{4}$). To determine the composition of as-synthesized LDPNCs, the elemental analysis was performed through energy-dispersive X-ray spectroscopy (EDS) in both scanning electron microscopy (SEM) and transmission electron microscopy (TEM), while the elemental mapping images and EDS spectra are shown in Figs. S2, S3 in the SI, respectively. The calculated stoichiometry of both CTIC and CTAC PNCs is highly consistent

with the nominal atomic ratio of Cs:Sn:M(III):Cl as 4:1:2:12, confirming that Sn(II) cations can be successfully coordinated in the LDP structure in the bulk case.

Surface properties and electronic structures

The surface chemical states of as-synthesized LDPNCs were investigated by measuring the X-ray photoelectron spectroscopy (XPS) spectra for each element, whose overall survey curves and respective core-level binding energies (BEs) are presented in Fig. S4 in the SI, and in Figs. 2a, b and S5, respectively. The Cs 3*d* and Cl 2*p* of CTIC are almost identical to those of CTAC PNCs in Fig. S5a–d, suggesting that the chemical states of Cs and Cl are insensitive to M(III) site substitution. The fit to the raw In $3d_{5/2}$ core level in Fig. S5e reveals two BEs, which attributed to the oxidation of In at 444.9 eV and 445.4 eV in different depths (ca. depth of less than 5 nm)[25,26]. The presence of these oxides of In is further evidenced by the fit to the O 1s core-level in Fig. S5g in the SI, where the component at the lowest BE (529.0 eV) is characteristic of the carboxyl group as a consequence of the capping ligands (i.e., OA^-)[27]. The remaining features, at 530.1 eV and 532.0 eV, have confirmed the aforementioned hypothesis on the presence of In_2O_3 in CTIC PNCs. More importantly, the Sn $3d_{5/2}$ of CTIC PNCs shows a clear one-component (Fig. 2a) that is solely assigned to the 2+ oxidation state at 486.8 eV[28]. On the other hand, in the case of CTAC PNCs, the Sn $3d_{5/2}$ surprisingly exhibits two distinct components (see Fig. 2b) with a 4+ oxidation state at 487.4 eV and a small amount of metallic Sn (i.e., Sn^0) at 485.2 eV, which are consistent with the previous works[29,30]. Additionally, the O 1*s* peak at the higher BE of 531.3 eV (see Fig. 2b) is another signature of the presence of Sn in the 4+ oxidation state (i.e., SnO_2)[31,32], while the O 1*s* core-level peak of 529 eV represents carboxyl species. Another deconvoluted XPS peak (at 530.4 eV) of CTAC PNCs in Fig. S5f, corresponding to the Sb $3d_{5/2}$ core-level, is characteristic of Sb in the 3+ oxidation state[33]. In comparison, the formation of a thin (up to 5 nm depth) In_2O_3 layer in CTIC (single PNC size is >40 nm) and the absence of Sb_2O_3 in CTAC can be explained by the fact that, on the Pauling scale, Sb is more electronegative than Sn, which in turn is more electronegative than In [23]. Therefore, when Sn and Sb are present simultaneously in the case of CTAC, the oxidation of Sn could be more favorable than the oxidation of Sb; however, when Sn and In are present within the same sample (i.e., CTIC), the oxidation of In becomes more favorable. Consequently, the thin In_2O_3 layer on the surface of CTIC PNCs is supposed to prevent the oxidation of Sn(II) to Sn(IV) in the LDP structure more effectively than the case of CTAC PNCs, which will be verified upon the stability test later. Although the formation of In_2O_3 and SnO_2 were observed on the surface states of CTIC and CTAC PNCs, respectively, our surface elemental analysis via XPS-based semi-quantitative atomic concentration (see Table S2 in the SI) still demonstrates the desired stoichiometry (4:1:2:12) of LDP structure in two cases, confirming the retention of Sn(II)-based LDP structure both in bulk and surface phases.

To gain insights into the interaction between the capping ligands (i.e., OA^- and OAm^+) and the surface of the LDPNCs, the X-ray absorption spectroscopy (XAS) measurements were conducted, from which several crucial structural information can be extracted upon the extended X-ray absorption fine structure (EXAFS) analysis (the extracted information is presented in Fig. S6 in SI)[34]. CTIC and CTAC PNCs demonstrate different *k* ranges of approximately 3 to 14 Å for the In and 3 to 13 Å for the Sb, respectively, as shown in Fig. 2c. Most scattering paths are located at the identical radial distance of 1.96 Å, indicating the highest coordination number at this distance. From the view of kink point position (see the inset in Fig. 2c), CTIC PNCs exhibit a slightly shorter bond length of In-Cl (1.45 Å) compared to that of the Sb-Cl bond (1.65 Å), although Sb^{3+} is more electronegative than In^{3+}. This may indicate that OAm^+ could interact with Cl^- more strongly in CTAC compared to the CTIC case. Meanwhile, we might have fewer structural disorders at a farther distance, approximately from 2.5 Å to 6 Å. In addition, we employed temperature-dependent (300–20 K) FT-IR spectroscopy to further confirm the influence of capping ligands on the surface properties of as-synthesized LDPNCs, with the IR spectra presented in Fig. 2d, e. The observed spectral region, ranging from 1200 to 1800 cm^{-1}, predominantly reflects the molecular vibration of the ligands (OA^- and OAm^+) on the surface of the PNCs, while lattice vibration is typically observed at lower frequencies. The characteristic vibrational band at 1468 cm^{-1} is assigned to the C-H symmetric bending mode of methylene groups with aliphatic hydrocarbon chains of OA^- and OAm^+, displaying a temperature-dependent shift and intensity change that signifies enhanced rigidity of the distorted lattice in both PNCs at decreasing temperature. The emerging peaks at 1377 cm^{-1} and 1401 cm^{-1} for CTIC are attributed to C-H symmetric vibrational bands, and the shift to 1369 cm^{-1} in CTAC indicates subtle changes in ligand binding interactions arising from lattice strain[19]. The vibrational bending centered at 1582 cm^{-1} for CTIC and shifted to 1620 cm^{-1} for CTAC reflects the N^+-H bending vibration that interacts with Cl-H as hydrogen bonding at the PNCs surface, suggesting stronger N-H ··Cl interaction in the Sb^{3+} system compared to the In^{3+} system, which is consistent with the previous EXAFS analysis. The present peaks at 1708 cm^{-1} and 1705 cm^{-1} are attributed to the stretching vibrations of the carbonyl (C = O) group. The shift of these bands to lower wavenumber is in agreement with the earlier analysis of the possible involvement of hydrogen bonding of the CTAC[35]. The observed peak at 1518 cm^{-1} in CTIC, which is absent in CTAC, corresponds to the symmetric vibration of N-H, which is likely influenced by the adjacent carbonyl group, suggesting a specific stretching interaction where carbonyl is bonded in the carbon framework and participates in hydrogen bonding[36].

To determine the electronic structures of Sn(II)-based LDPNCs, we performed density functional theory (DFT) calculations using PBE for structural optimization and PBE0(α) hybrid functionals for the reference gap values, where α was determined from the Koopmans condition for each compound (see the Methods for details). The calculated band structures and density of states (DOS) for CTIC and CTAC are shown in Fig. 2f, g. The band dispersions were obtained at the PBE level and rigidly shifted to reproduce the corresponding PBE0(α) band gaps, since fully converged hybrid-functional band structures along dense high-symmetry paths were computationally too demanding for the present systems. Both compounds exhibit semiconducting behavior, with indirect fundamental gaps and direct transitions lying only modestly higher in energy. The calculated indirect bandgaps are 3.79 eV for CTIC and 3.40 eV for CTAC, while the corresponding direct bandgaps are 4.11 eV and 3.54 eV, respectively. The relatively small energy separation between the indirect and direct transitions, particularly for CTAC (~0.14 eV), suggests a quasi-direct bandgap character. In CTIC, this difference is somewhat larger (~0.33 eV), yet still small enough that direct optical transitions remain accessible. To understand the electronic origin of these different bandgaps, we analyzed the projected DOS. The valence-band region in both materials is dominated primarily by Cl 3*p* states, with minor contributions from Sn 5*s* orbitals. In contrast, the conduction-band edge is formed by hybridized Sn 5*p* and Cl 3*p* states, together with contributions from In 5*s* states in CTIC and Sb 5*p* states in CTAC. These results suggest that the different M(III)-site orbital contributions near the conduction-band edge, namely In 5*s* in CTIC and Sb 5*p* in CTAC, are associated with the smaller calculated bandgap of CTAC. The scissor-corrected PBE bands also suggest somewhat greater conduction-band dispersion in CTAC, although this comparison should be interpreted qualitatively.

To further refine the comparison between theory and experiment, we verified the influence of thermal fluctuations, spin-orbit coupling (SOC), and free-exciton binding on the bandgaps. Thermal effects were estimated from 10-ps-long molecular dynamics simulations performed within CP2K[37] at the PBE[38] level for computational efficiency. Finite-temperature MD indicates a negligible thermal renormalization of the gap for both materials at this level of theory, with the time-averaged gap differing by less than 0.01 eV from the 0 K value. The role of SOC was then evaluated in VASP by comparing PBE calculations with and without SOC, showing a negligible effect for CTIC and a more pronounced reduction for CTAC (−0.27 eV). Finally, free-exciton binding energies were estimated using TDDFT[39] at the PBE0(α) level in VASP, yielding values of 0.31 eV for CTIC and 0.35 eV for CTAC. Starting from the calculated direct bandgaps (4.11 eV for CTIC and

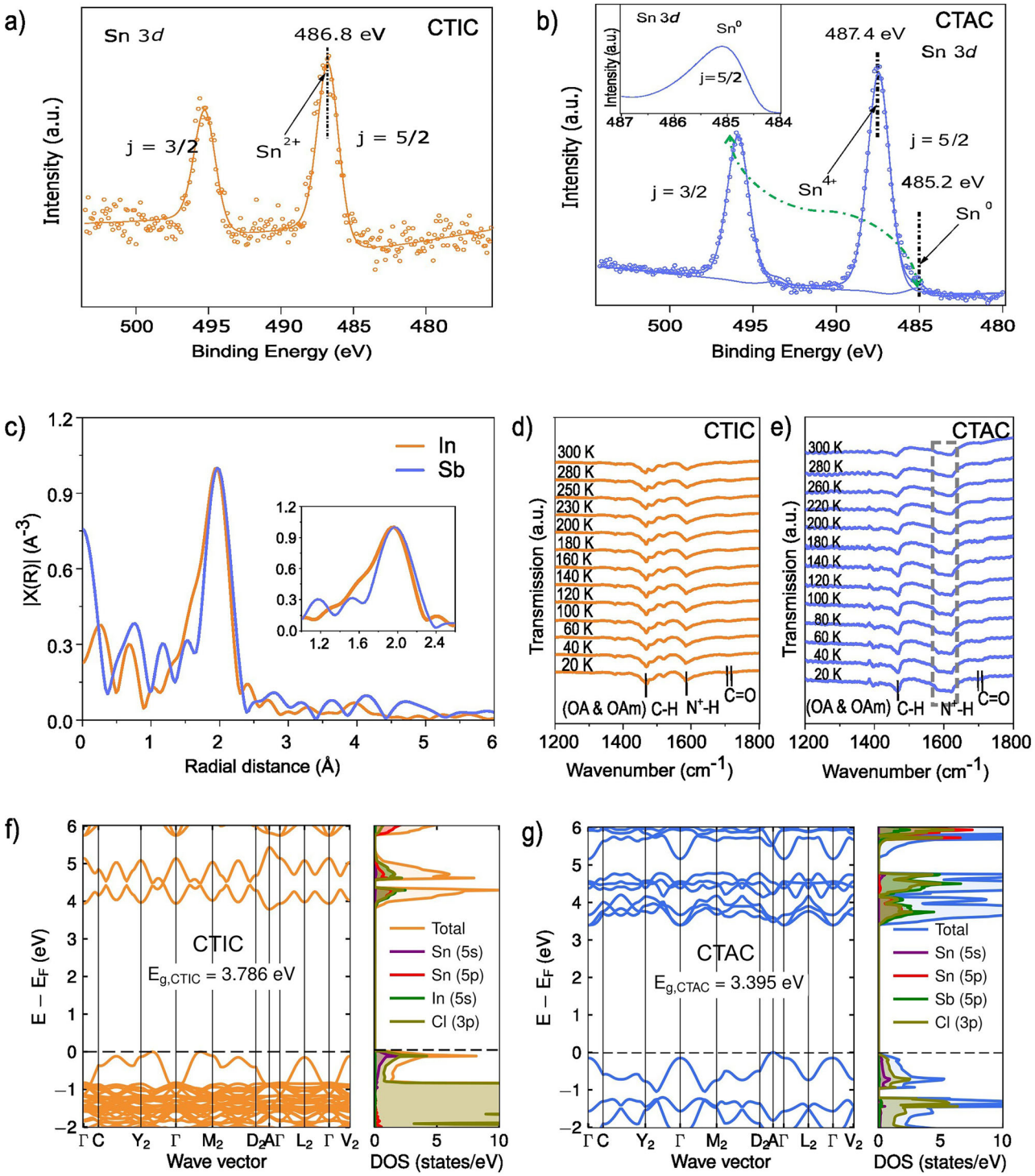

Fig. 2 | Oxidation state of Sn and atomic environment. XPS spectra of **a** CTIC and **b** CTAC PNCs for Sn element. **c** EXAFS spectra of LDPNCs with fittings in *R*-space. The inset presents the magnified spectra in the early range of *R*-space. **d**, **e** Temperature-dependent IR transmission spectra of capping ligands (OA^- and OAm^+) coordinated with LDPNCs. **f**, **g** Calculated band structures and density of states (DOS) of CTIC (left panel) and CTAC (right panel). Both band structures and DOS are obtained at the PBE level and corrected by a rigid scissor shift of the conduction bands to match the PBE0 band gaps. The dash lines represent the Fermi energy which is set to 0 eV.

3.54 eV for CTAC), these corrections lead to estimated direct optical gaps of approximately 3.80 eV for CTIC and 2.92 eV for CTAC.

The valence bands of CTIC and CTAC PNCs were also experimentally determined through the cyclic voltammetry (CV) measurements (see the CV setup details in the Methods). To determine the electronic band structure of the PNCs, the valence band (VB) and conduction band (CB) edge positions were calculated using electrochemical measurements referenced to the ferrocene/ferrocenium (Fc/Fc^+) redox couple. The Fc/Fc^+ energy level was taken as 4.8 eV relative to the vacuum level. The VB energy (E_{VB}) was calculated using $E_{VB} = -(V_{ox} - V(Fc/Fc^+) + 4.8)$ eV, where V_{ox} is the onset oxidation potential of the sample, and $V_{Fc/Fc+}$ is the mid-point potential of the ferrocene standard. The CB energy (E_{CB}) was then

derived from the relation $E_{CB} = E_{VB} + E_g$, where E_g represents the optical bandgap of LDPNCs[19]. The onset oxidation potential of CTIC (1.32 V vs Ag/AgCl) is slightly higher than that of CTAC (1.10 V vs Ag/AgCl), suggesting that CTIC PNCs possess improved resistance toward oxidation. This difference indicates that substitution at the M(III) octahedral site influences the electronic structure and redox behavior of the LDP framework, as shown in Fig. S7a, b. According to the potential conversion formula Equation (see in the Methods), the VB energies of CTIC and CTAC PNCs were calculated to be −5.97 and −5.75 eV vs. vacuum. Moreover, based on the Tauc plot analysis of UV–Vis absorption spectra (Fig. S7c), the optical bandgaps of two PNCs were determined to be 2.64 eV for CTAC and 3.77 eV for CTIC. These values are reasonably in agreement with the direct optical band gaps estimated from DFT calculations, namely 2.92 eV for CTAC and 3.80 eV for CTIC. The diffuse nature of Sb orbitals contributes to a decline in energy separation between the VB and CB, attributed to the more delocalized character of Sb 5*p* orbitals, which also shows a lower Urbach energy of CTAC compared to CTIC, as shown in Fig. S8a, b. Consequently, the CB energies of CTIC and CTAC PNCs were calculated to be −-2.20 and −-3.11 eV, respectively. All band structure properties (extracted from both experimental and simulated results) are compared in Fig. S7d as well as summarized in Table S3 in the SI.

Optical and photophysical properties

The PL properties of as-synthesized LDPNCs in the solid state were determined upon the measurements of emission spectra, by exciting the PNC films at 375 nm. Surprisingly, only CTIC PNCs exhibit a detectable PL profile (see Fig. 3a), while no obvious PL was observed in the case of CTAC PNCs. The asymmetric emission peak centered at 529 nm, together with the large Stokes shift (~250 nm), indicates strong lattice relaxation and carrier self-trapping in the CTIC PNCs. This emission possibly originates from localized excited states associated with the isolated $[InCl_6]$ octahedron units[40,41]. However, the $[SbCl_6]$ octahedron in CTAC PNCs in turn triggers the relaxation of the photoexcited states more in a nonradiative way (dark transition), indicating a different excited-state relaxation pathway compared to CTIC PNCs. Accordingly, the relative PLQY of CTIC PNCs (vs. Rhodamine B dye film as the reference, see Fig. S9 in the SI) was extracted to be almost 12%, slightly outperforming the previous reported record of 11.4% for lead-free LDPNCs[18]. The time-resolved PL (TRPL) decay of CTIC PNCs was monitored at the emission peak (~529 nm) that was fitted well by a tri-exponential function (see the fitting results in Fig. 3b). The fitted average lifetime (τ_{AVG}) is around 1 ns that is faster than the long-lived PL lifetimes (e.g., a few hundreds of ns or even sub-μs) of standard STEs, which confirms the simulated results regarding the assignment of relaxation of localized excited states in early timescale, i.e., self-trapped excited states[17,19].

To determine the photophysical properties of both PNCs, we performed the excitation (at 400 nm) power-dependent ultrafast transient absorption (TA) measurements on the LDPNCs films. The 2D TA spectral maps of CTIC and CTAC PNCs under an excitation power of 0.4 mW (equivalent to an energy intensity of 7.86 μJ/cm^2) are compared in Fig. 3c, d, respectively, while other TA spectral maps under diverse excitation powers are presented in Fig. S10 (for CTIC) and Fig. S11 (for CTAC) in the SI. Both PNCs demonstrate quite distinct TA spectral profiles at different time delays. Specifically, CTIC PNC film features a very broad positive photo-induced absorption (PIA) band centered at ~600 nm that covers almost the whole visible to NIR range (380 to 900 nm) within the detection limit, of extensive excited-state localization/self-trapping in the lattice of CTIC PNCs, namely STE-like states that have been observed for similar In-based LDPNCs previously[19]. In contrast, a relatively narrow PIA band centered at ~400 nm that corresponds to the first exciton peak (see the absorption spectrum in Fig. 3a) was only observed in the TA spectra of CTAC PNCs. This indicates that excited-state dynamics in CTAC are dominated by band-edge and/or dark relaxation channels, lack of the formation of STE or STE-like states. Since there is no observed emission from CTAC PNCs, it means most photo-generated excitons relax nonradiatively[42]. A change in the excitation power at 400 nm plays a role in influencing the evolution of TA spectral shape and peak position in addition to the TA intensity in a change of optical density (i.e., ΔO.D.), particularly for CTIC PNCs. With the increase in the excitation power (0.3 to 0.45 mW), a slight blue shift was observed in the TA spectra of CTIC PNCs throughout the time delays. This suggests that more energy input from the excitation source results in the additional energy transfer from free excitons to STE-like (i.e., self-trapped excited state), reflected in the blue shift in the TA spectra of CTIC PNCs towards higher energy conversion. However, in the case of CTAC PNCs, due to the much less formed self-trapped excited state, the increasing excitation power only magnified the TA spectral amplitude without an obvious change in the TA band position.

We then turn to assess the charge carrier dynamics of both PNCs by comparing the TA decays of CTIC (at 600 nm) and CTAC (at 400 nm) under the excitation power of 0.4 mW, as shown in Fig. 3e. The excitation power dependent TA decays for both LDPNCs are also compared in Figs. S12 and S13, respectively. All normalized TA decays were fitted well with a tri-exponential function, and the fitting results are summarized in Table S4 in the SI. The ultrafast TA signal growth within 0.5 ps indicates a transition from free excitons either to STE-like trapping for CTIC or to intraband trapping for CTAC[17]. For the relaxation of STE-like states in CTIC PNCs, two fast processes that consist of an ultrafast component (t_1 of <1 ps) and a medium-fast component (t_2 of <35 ps), were assigned to the nonradiative recombination, while a slow component (t_3 of >4 ns) corresponded to the radiative recombination of self-trapped localized excited states that eventually contributes to the PLQY of 12% as observed above[40]. Interestingly, the increase in the excitation power can extend the average decay lifetimes of CTIC PNCs by particularly prolonging the slow component up to ~5.2 ns, revealing that the increasing density of photo-generated self-trapped excited states may positively influence the radiative recombination towards longer excited states. However, the charge dynamics of CTAC PNCs differ from the case of CTIC PNCs, in which three components were assigned to bimolecular recombination (the first two fast components of t_1 and t_2) and to trap-assisted nongeminate recombination (the slow component of t_3), respectively[43–45]. Notably, the average lifetimes of excitation power-dependent TA decays for CTAC range from 11 to 16 ns, which are almost three times longer compared to those of CTIC PNCs. Because no PL signal is observed from CTAC, we speculate that the recombination processes of this type of Sn-based LDPNCs are partially driven by the non-radiative self-trapped excited states. The long-lived TA decay lifetimes of CTAC PNCs plausibly stem from the fewer traps (surface or bulk) in the band edge structure, which can be beneficial for efficient charge transfer in the photocatalytic reactions. The overall scheme of charge transport dynamics of both CTIC and CTAC PNCs is summarized in Fig. 3f.

To further examine the excited-state relaxation pathways, we performed modeling of localized excited states in the ideal structures, including hole polarons, electron polarons, and fully localized STE-like configurations (see Section S12, Fig. S15, and Table S7 in the SI). Both CTIC and CTAC were found to support such localized states, indicating that self-trapping is not unique to the In-based compound. At the same time, the calculated emission energies of the fully localized STE-like states lie far below the observed visible PL, suggesting that the measured CTIC emission does not originate from the deepest fully relaxed minimum. These results therefore suggest that the visible PL is more plausibly associated with a higher-lying self-trapping-related state, whereas in CTAC this emissive pathway is outcompeted by dark relaxation channels in the real nanocrystal system.

Structural and colloidal stability

As one key hypothesis of quasi-2D LDP structure, the inserted M(II) octahedron layer, i.e., Sn(II) octahedron layer in this work, can be effectively protected by two adjacent M(III) octahedron layers, i.e., In(III) or Sb(III), against the penetration and oxidation of O_2 and H_2O molecules. We thus monitored the evolution of the XRD patterns of two PNCs in film state that were stored in dark ambient conditions (25 °C and RH ≈ 60%), as compared in Fig. 4a (for CTIC) and 4c (for CTAC), respectively. Notably, the XRD patterns of the CTIC PNCs film can retain the major feature of those

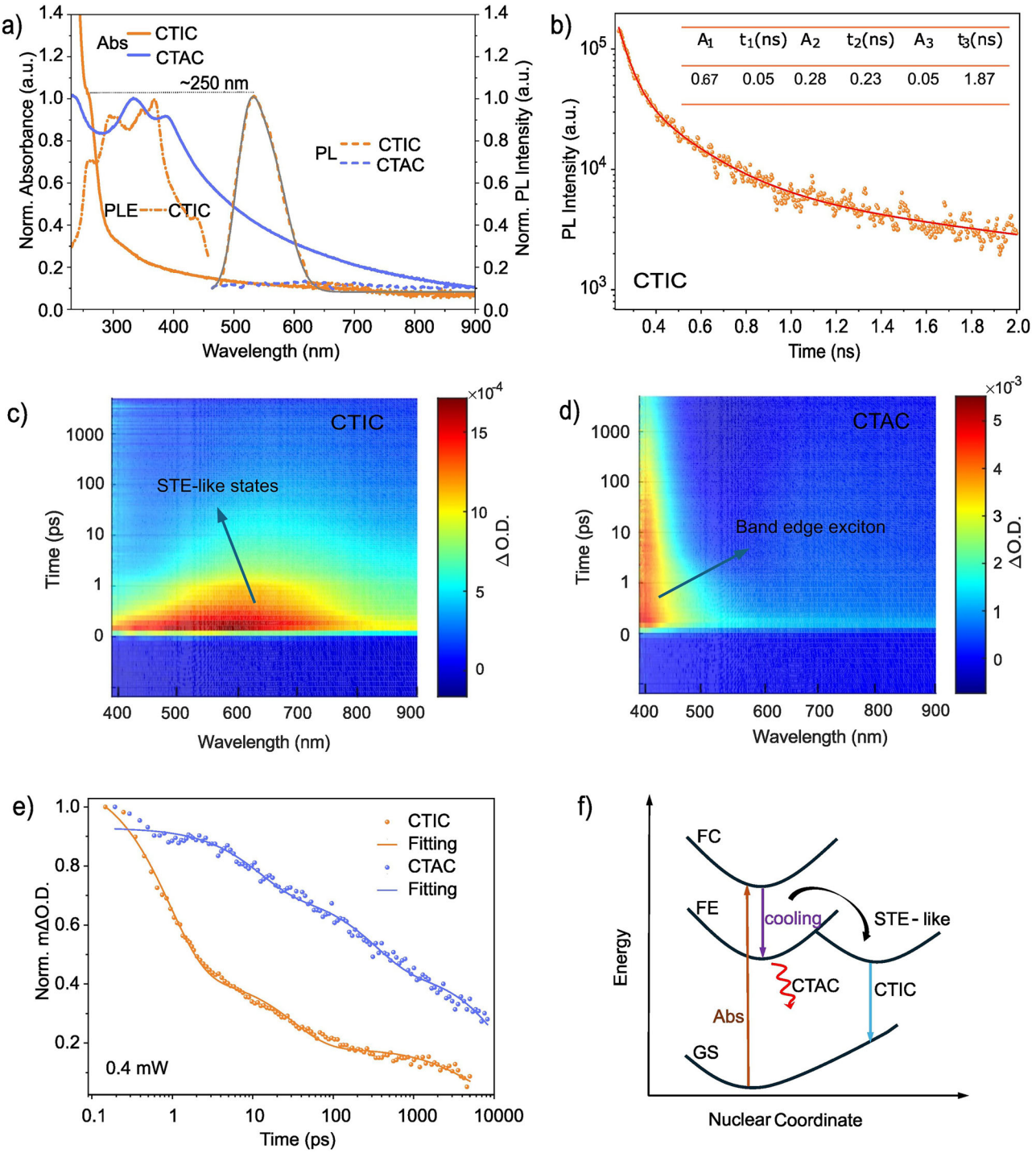

Fig. 3 | Optical properties and charge dynamic analysis. a Optical (absorption and emission) spectra of CTIC and CTAC PNCs films. The dashed line shows the PL excitation (PLE) spectrum, monitoring at the emission peak of 529 nm for CTIC PNCs. **b** Time-resolved PL (TRPL) decay of CTIC PNCs. The inset presents the fitting results upon a tri-exponential function. **c**, **d** Contour plots of LDPNCs in transient absorption (TA) spectra. The PNCs films were excited at 400 nm with an excitation power of 0.4 mW. **e** Normalized TA decays for both LDPNCs under the excitation power of 0.4 mW, monitored at 400 nm for CTAC and at 600 nm for CTIC, respectively. ΔO.D. is the change of optical density. The solid line presents the fitted curve upon $\triangle O.D = A_1 \exp\left(-\frac{t}{\tau_1}\right) + A_2 \exp\left(-\frac{t}{\tau_2}\right) + A_3 \exp\left(-\frac{t}{\tau_3}\right)$. **f** Configuration coordinate diagram for the STE-like state mechanism of LDPNCs. GS ground state, Abs light absorption, FC free carrier state, FE free exciton state.

characteristic peaks even after more than 300 days of storage, although the intensity of peaks was observed to gradually decrease (see the magnified peaks of 28°−30° in the right panel of Fig. 4a). This clearly suggests that the LDP structure has been effectively maintained upon the significant hindering of oxidizing Sn(II) to Sn(IV) in the bulky case of CTIC PNCs, to the best of our knowledge, which exhibits the longest structural stability of Sn(II)-based perovskites. On the contrary, the CTAC PNCs film demonstrates a much-accelerated change in the evolution of XRD patterns right after around 25 days, by observing a clear swapping phenomenon of several satellite peaks, e.g., 24–25° for $(\bar{3}11)$-(020), 28–30° for (022)-(400), 32–34° for $(40\bar{4})$-$(2\bar{2}2)$. More interestingly, after around 100 days of storage, the as-swapped weaker satellite peaks disappeared (see one example in the range

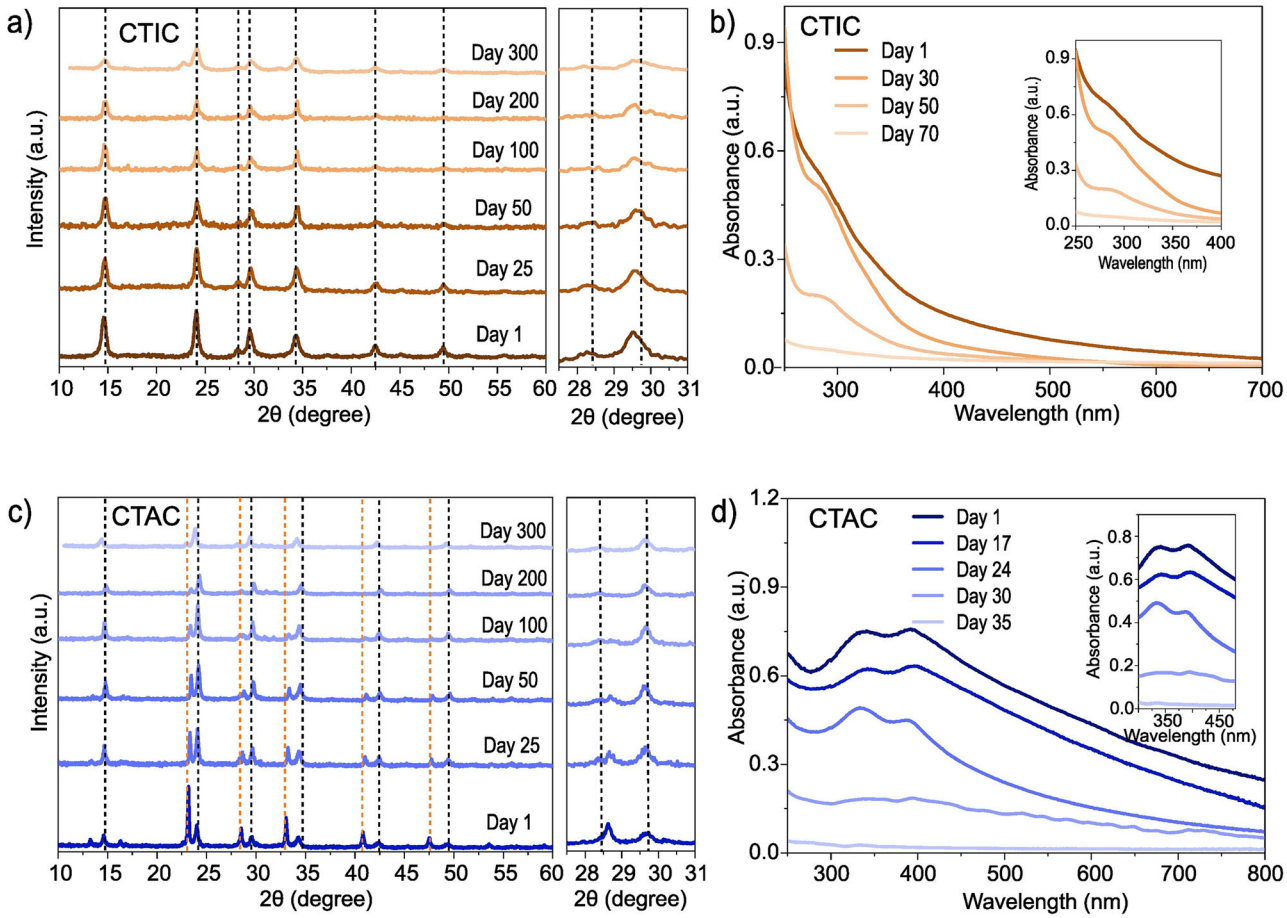

Fig. 4 | Structural and colloidal stability study. Evolution of XRD patterns of **a** CTIC and **c** CTAC PNCs in film state vs. various storage times (by days). Evolution of absorption spectra of **b** CTIC and **d** CTAC PNCs in suspension. Both films and suspensions were stored in dark ambient conditions.

of 28–30° in the right panel of Fig. 4c). Such distinct behavior in the evolution of XRD patterns of CTAC PNCs reveals that Sn(II) can still be oxidized to Sn(IV) in the LDP structure upon the diverse selection of M(III) site, i.e., Sb(III) octahedron layers exhibit less protection effect compared to In(III) counterparts. This in turn agrees with previous XPS data that the electronegativity of the M(III) site as one additional factor indeed influences not only the surface oxidized state but, to some extent the bulky oxidized state as well in the LDP structure. We then investigated the morphological stability of LDPNCs after >300 days of storage in ambient conditions, with the TEM images shown in Fig. S16 in the SI. It is clearly noted that the aged CTIC PNCs exhibit an irregularly around morphology compared with the hexagonal shape of the fresh case (see Fig. 1c), which appear partially amorphous with a noticeable increase in the size. Likewise, the aged CTAC PNCs are obviously more aggregated with a big chunk shape, showing even lower crystallinity compared to the CTIC ones. In both cases, their lattice fringes are hardly resolved, which is in agreement with the XRD comparison of aged PNCs. To confirm colloidal stability, we further measured the steady-state absorption spectra of two PNCs in suspension regularly after periodic storage in dark ambient conditions, as shown in Fig. 4b (for CTIC) and 4 d (for CTAC). Similar to the trend of structural stability, CTIC PNCs lost the feature of the first exciton peak at ~280 nm (see the inset magnified spectra) after 70 days of storage, while it just took 35 days in the case (disappearance of the first exciton peak at ~400 nm) of CTAC PNCs. The observed higher colloidal (optical) stability of CTIC PNCs suggests that two adjacent In(III) octahedron layers can more effectively inhibit the oxidation or decomposition of the middle Sn(II) octahedron layer, when compared with the CTAC PNCs suspension. We assume that the fast quenching of the absorption confirms the oxidation on the surface, where the typical absorption of these PNCs stems from the electronic transition of In-Cl and Sb-Cl, respectively. Similar phenomena were also observed in several other In- and Sb-layered double perovskites[15,17–19]. This means, in this LDP system, the M(III) site is likely to play a role as a sensitizer component, with a prominent absorption capability. Therefore, we observed that the relatively rapid oxidation of Sn significantly reduced CTAC absorption.

Photoelectrochemical (PEC) performance

This type of LDPNCs has been reported to be suitable for photocatalytic oxidation[16] or PEC redox reactions with organic compounds as the intermediate materials due to their featured quasi-2D layered structure for a large interfacial area as extensive reaction sites[19]. A typical PEC cell was fabricated by utilizing a standard three-electrode system (see the setup and reaction scheme in Fig. 5a, b), which consists of PNC film/c-TiO_2/FTO as a working electrode (WE) with an active area of ~2 cm^2, Pt as a counter electrode (CE), and Ag/AgCl as a reference electrode (RE), respectively. A solution of 0.1 M tetrabutylammonium hexafluorophosphate ($TBAPF_6$) in anhydrous dichloromethane (DCM) was employed as the electrolyte, where 4 mM benzoquinone was added as the redox reactant. The proposed PEC-induced redox reactions based on the LDPNC films as the photoanode include three sub-reactions: (i) Reduction at CE: $C_6H_4O_2 + e^-$ (photogenerated) → $C_6H_4O_2^{\cdot-}$; (ii) Oxidation at WE: $C_6H_4O_2 + h^+$ (photogenerated) → $C_6H_4O_2^{\cdot+}$; (iii) Within electrolyte: $C_6H_4O_2^{\cdot+} + C_6H_4O_2^{\cdot-} \rightarrow C_6H_4O_2$[19]. Specifically, upon 1 Sun illumination (AM 1.5 G, 100 mW cm^{-2}), the photogenerated charge carriers separate at the interface of LDPNC film and TiO_2 at WE, where the extracted electrons further transfer to the FTO substrate, then to CE through the external circuit, for reducing the benzoquinone to anion radical, as presented in formula (i). On the other side, the left photogenerated holes on the

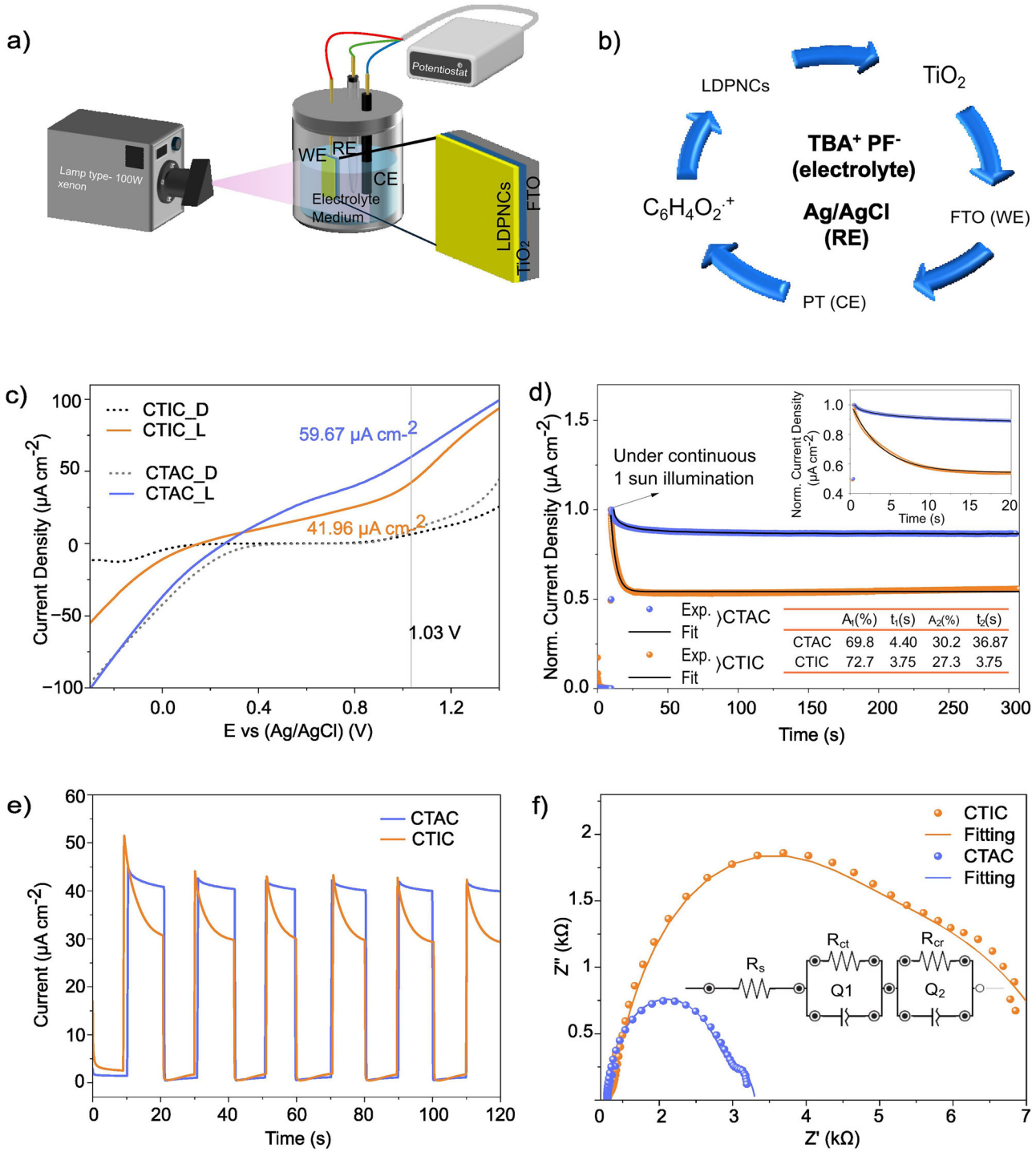

Fig. 5 | Photoelectrochemical properties during the photo-induced redox reaction. a A layout of the PEC cell based on LDPNC film as the photoanode in a three-electrode system. **b** Cyclic scheme of photoelectrochemical-induced redox reactions. **c** Current density (*J*) vs. applied potential (*V*) (vs. Ag/AgCl) curves for LDPNCs-based photoanodes under dark (dash line) and 1 Sun (solid line) conditions. **d** Normalized transient photocurrent density decays for LDPNC-based photoanodes under continuous 1 Sun illumination at 1.03 V. The solid line presents the fitted curve with a biexponential function: $I(t) = A_1 \exp\left(-\frac{t}{\tau_1}\right) + A_2 \exp\left(-\frac{t}{\tau_2}\right)$. **e** Light on-off (interval time: 10 s) traces of photocurrent density at a constant applied potential of 1.03 V. **f** Nyquist plots of EIS curves, fitted by using a simple equivalent circuit model (presented in inset).

surface of the LDPNC film tend to oxidize the benzoquinone into several potential products, e.g., benzoquinone cation radical, as presented in formula (ii)[19,46,47]. This redox reaction occurs under an applied potential of 0.8 V vs. Ag/AgCl, which is the onset position of the dark *J*—*V* curve (see Fig. 5c). Prior to the measurement, we compared the thickness-dependent current as shown in Table S8, which exhibits an optimal film thickness of approximately 200 nm for TiO_2 and 500 nm for PNCs. We then extracted the photocurrent densities (*J*) of 41.96 μA cm^{-2} and 59.67 μA cm^{-2} for CTIC and CTAC PNCs at 1.03 $V_{Ag/AgCl}$ (equivalent to 1.23 $V_{RHE,}$ which is the redox potential for water splitting reaction)[48], respectively. To the best of our knowledge, the almost 60 μA cm^{-1} @1.03 $V_{Ag/AgCl}$ from CTAC PNCs is the highest value among all LDP-based PEC reactions as well as at the top level of all lead-free PNCs-

based PEC performance, as compared in Table S9 in the SI. To confirm the response rate of photogenerated currents between two PNCs, the transients of photocurrent density at a constant potential (i.e., 1.03 $V_{Ag/AgCl}$) under continuous 1 Sun illumination were measured and compared in Fig. 5d. The transient decays can be fitted well with a bi-exponential function, showing two contributed components (t_1 and t_2).We assign the fast component (t_1) to the initial carrier trapping/detrapping process and the slow component (t_2) to the interfacial charge recombination kinetics, respectively. CTIC accordingly demonstrates slightly faster photoresponse time ($t_1 = 3.7$ s) than that ($t_1 = 4.4$ s) of CTAC PNCs, corresponding to moderately accelerated carrier trapping/detrapping process upon the shallow traps. The noted big reduction in the amplitude of photocurrent density before photoinduced stabilization along with much faster second component ($t_2 = 3.8$ s) in case of CTIC PNCs, hints that the interfacial charge recombination dynamics can be effectively hindered in turn in case ($t_2 = 36.8$ s) of CTAC PNCs, which is plausibly attributed to the higher carrier (particularly hole) mobility towards the interface of CTAC and electrolyte[49]. We further investigated the stability of photocurrent under repeatable light-on/off conditions with an internal switching time of 10 s, as shown in Fig. 5e. Interestingly, both PNCs exhibit relatively stable and reproducible photocurrents upon more cycles of light-on/off, demonstrating good photo-response stability.

To gain more insight into the generation of diverse photocurrents, we conducted electrochemical impedance spectroscopy (EIS) measurements to clarify the (photo)electrical properties of CTIC and CTAC PNCs in the film state. Figure 5f demonstrates the Nyquist plots of EIS spectra with an equivalent circuit model shown in the inset, where R_s is the series resistance, R_{ct} is the charge transfer resistance, and R_{cr} is the recombination resistance.

In theory, the different semicircle reflects variable interval charge transport kinetics; a smaller diameter in the first semicircle (corresponding to the high frequency region) indicates efficient charge transfer; thereby, a larger semicircle in the second semicircle (corresponding to the low frequency region) suggests slow charge recombination[50]. Intriguingly, CTAC PNCs possess much lower R_{ct} (432 Ω) than that (2689 Ω) of CTIC, leading to more efficient charge transfer with higher carrier mobility that is in good agreement with the previously observed higher photocurrent and faster photo-response in the case of CTAC PNCs, although the R_{cr} (1597 Ω) of CTAC is about half of that (3840 Ω) of CTIC NCs, which possibly plays a minor role in overall charge transport dynamics. All PEC properties of LDPNC-based photoelectrodes are summarized in Table S10 in the SI.

Discussion

Quasi-2D layered double perovskites have recently emerged as one promising lead-free alternative absorber that can potentially fulfill the requirement of both performance and stability, due to their relatively good optoelectronic properties (e.g., direct bandgap nature and low effective masses) and outstanding M(II) site structural stability that benefits from the featured vacancy layers between unit cells as well as the sandwiched octahedral structure of M(III)/M(II)/M(III) within a unit cell. This has inspired us to coordinate Sn(II) still as the closest Pb(II) analogous divalent cation, into the LDP structure as the M(II) site in this work. Upon the successful synthesis of colloidal $Cs_4Sn(II)M(III)_2Cl_{12}$ PNCs, several intriguing electronic and surface properties have been disclosed. First, the direct bandgap of CTAC PNCs ($E_g = 2.64$ eV) is lower than that of CTIC PNCs ($E_g = 3.77$ eV), hinting that the band structure of this type of LDPs is dominated by M(III) site cations, which is also supported by our DFT calculations. The featured self-trapped excited states can also be tailored upon M(III) site-driven lattice engineering. A relatively bright self-trapping-related emission (PLQY ~ 12%) has been observed from CTIC PNCs, while almost no emission can be detected from CTAC PNCs. Additional calculations on localized excited states show that both CTIC and CTAC can support hole polarons, electron polarons, and fully localized STE-like configurations. Thus, the absence of PL in CTAC cannot be attributed simply to the lack of self-trapping. At the same time, the calculated emission energies of the fully localized STE-like states lie far below the measured visible PL, indicating that the experimentally observed CTIC emission is unlikely to originate from the deepest fully relaxed minimum. Instead, the visible PL is more plausibly associated with a higher-lying self-trapping-related state. In CTAC, this emissive pathway is likely outcompeted by dark relaxation channels, consistent with its pronounced low-energy sub-gap absorption and the XPS evidence of Sn oxidation. On the other hand, when employing these LDPNCs as the photoanode for PEC redox reactions with benzoquinone, CTAC PNCs in turn exhibit higher photocurrent generation with faster photo-response time compared to the CTIC counterparts. This suggests that the light harvesting or external quantum efficiency (EQE) determines the level of photogenerated current in this work, since the narrower bandgap of CTAC PNCs could easily absorb more photons in the visible range, although the as-formed STE-like states do not contribute to the red emission. More importantly, our long-term structural stability tests (time-dependent XRD evolution data) have confirmed our hypothesis that this LDP structure can indeed protect the middle Sn(II) octahedron layer against the ambient oxidation to Sn(IV) with two adjacent M(III) octahedron layers, at least in the bulk case. Regarding the surface states of LDPNCs, our comprehensive XPS analysis verifies a trade-off situation between Sn^{2+}, In^{3+} and Sb^{3+} cations that the electronegativity acts as one more factor to influence their oxidized states, resulting in the observation of Sn(IV) only in Sb-based PNCs (CTAC) but not in In-based PNCs (CTIC); however it is only applicable within the depth of ~5 nm from the very surface of LDPNCs. We believe this work paves the way for simultaneously enhancing the optoelectronic properties and structural stability of highly attractive Sn(II)-based perovskites through further diverse engineering (e.g., halide engineering, doping engineering) on a promising quasi-2D LDP structure.

Methods

Materials

Indium(III) acetate ($In(OAc)_3$, ≥99.99%), antimony(III) acetate ($Sb(OAc)_3$, 99.99%), oleic acid (OA, technical grade, 90%), oleyamine (OAm, technical grade, 70%), 1-octadecene (ODE, technical grade, 90%), chlorotrimethylsilane (TMS-Cl, ≥99.9%), tetrabutylammonium hexafluorophosphate (TBAPF, ≥99.99%), titanium(IV) iso-propoxide (TTIP, 97%), and 1,4-benzoquinone (BQ, 98%) were purchased from Merck. Tin(II) acetate ($Sn(OAc)_2$, 99.99%) was purchased from Ambeed. Cesium acetate (CsOAc, 97%) and dichloromethane (DCM, 99.6%) were purchased from Thermo Scientific. Hexane (analytical grade, 99.2%) and isopropanol (IPA, technical grade, 70%) were purchased from VWR. The FTO was purchased from OPV tech with a thickness of 2.2 mm and sheet resistivity between 6 and 8 ohm/sq. All chemicals were purchased without further purification.

Synthesis of $Cs_4SnM(III)_2Cl_{12}$ LDPNCs

Colloidal $Cs_4SnM(III)_2Cl_{12}$ PNCs were synthesized through a modified hot-injection method[15]. CsOAc (68.1 mg, 0.35 mmol), $Sn(OAc)_2$ (29 mg, 0.125 mmol), $In(OAc)_3$ (72.99 mg, 0.25 mmol) or $Sb(OAc)_3$ (74.73 mg, 0.25 mmol) were mixed with OA (1.25 mL), OAm (0.33 mL) and ODE (5.00 mL) in a 25 mL three-neck flask. All the precursors were homogeneously stirred at room temperature prior to several purging cycles (2–3) between nitrogen and vacuum, which were then heated to 120 °C for 1.5 h under vacuum. After all the precursors were well dissolved, the mixture solution turned out to be a pale and transparent yellow color. The crude solution was then further heated to 180 °C for CTIC (230 °C for CTAC) in a nitrogen atmosphere. Upon reaching the target temperature, 0.3 mL TMS-Cl was swiftly injected into the crude solution, and the solution was swiftly turned to cream for CTIC and yellow for CTAC, demonstrating the formation of the PNCs. The solution was kept under three flask necks for 5 s to quench further PNCs growth, and then the reaction was quenched by quickly moving the flask into a water/ice bath until it cooled down to 40 °C. The crude solution was collected and washed with an equivalent volume of mixture solvent of hexane and isopropanol (v:v = 1:1), followed by centrifugation for 5 min at 7500 rpm. After discarding the supernatant, the precipitates (white for CTIC; yellow for CTAC) were completely dried for further characterization (dispersed in hexane or toluene) or fabrication[25].

Fabrication of LDPNC-based PEC cells

The fabrication of the PNCs-coated photoelectrodes began with cutting fluorine-doped tin oxide (FTO) into a size of 2.5 × 2.5 cm. Subsequently, the FTO was washed with soap and water using a brush, then cleaned with technical-grade acetone (VWR) and technical-grade 2-propanol (VWR) in sequence. After the substrates are dry, a compact TiO_2 (c-TiO_2) layer is deposited onto cleaned (FTO) glass substrate via the spin coating method. A sol-gel-derived 1.46 M TiO_2 (Titanium (IV)) isopropoxide (TTIP, 97%, Merck) diluted in 2-propanol (≥99.8%, Merck) and HCl (37%, VWR) was spin-coated onto the FTO at 2000rpm for 35 s, followed by annealing treatment at 450 °C for 30 min. Subsequently, 0.15 mg/ml of LDPNCs was deposited onto the pre-coated TiO_2 layer by spin coating at 4000 rpm for 35 s. For the electrolyte system, the solution was prepared using DCM as the solvent, benzoquinone (4 mM) as the redox intermedium, and 0.1 M $TBAPF_6$ as the supporting electrolyte. One typical PEC cell was assembled using a platinum wire as the CE, an Ag/AgCl electrode as the RE, and the as-prepared LDPNCs/c-TiO_2/FTO substrate (active area: ~2 cm^2) as the WE. The LDPNC-based photoanode was directly attached to the electrolyte solution under 1 Sun illumination.

DFT calculations

First-principles calculations based on DFT were carried out using a periodic model as implemented in the Vienna Ab Initio Simulation Package (VASP 6.4.2)[51–53]. The projector augmented-wave (PAW) method[54,55] was employed to describe the interactions between electrons and ionic cores, where Cs $5s^25p^66s^1$, Sn $5s^25p^2$, In $4d^{10}5s^25p^1$, Sb $5s^25p^3$, and Cl $3s^23p^5$ were treated as valence electrons. Their wavefunctions were expanded using a plane-wave basis with a cutoff energy of 500 eV. The exchange-correlation functional was approximated using the generalized gradient approximation (GGA) in the form of Perdew, Burke, and Ernzerhof (PBE)[38]. All structures were optimized using the conjugate gradient method[56]. A Gaussian smearing technique ($\sigma = 0.05$ eV) was used during structural relaxations, where the calculated energies were extrapolated to zero smearing width.

The unit cells of CTIC and CTAC were obtained from experimentally determined crystallographic data, and their primitive cells ($Cs_4SnIn_2Cl_{12}$ and $Cs_4SnSb_2Cl_{12}$) were subsequently optimized using the PBE functional. The Brillouin zone was sampled using a Γ-centered 5 × 5 × 3 k-point mesh for the structural relaxation of both systems. The structures were fully relaxed until the force acting on each atom was less than 0.01 eV/Å. The energy convergence criterion was set to 1×10^{-6} eV. The structural optimization yielded more symmetric coordination environments with reduced octahedral distortions (see Fig. S14), and the relaxed geometries are therefore considered representative of the intrinsic atomic configurations for evaluating their electronic properties. The calculated lattice parameters are summarized in Table S5.

Subsequently, electronic structure calculations were performed using the PBE0 hybrid functional[57], with the fraction of exact Hartree-Fock exchange determined via the Koopmans' condition[58]. This approach yielded optimal exchange fractions of approximately 33.3% for CTIC and 32.5% for CTAC, reflecting the dielectric screening in the materials. The density of states (DOS) was calculated using the tetrahedron method with Blöchl corrections[59], employing a Γ-centered 5 × 5 × 3 k-point mesh. Hybrid-functional gap values were obtained explicitly, whereas the band dispersions shown in the main text were evaluated at the PBE level and aligned to the hybrid gap by a rigid scissor shift. Band structures were calculated along high-symmetry paths in the Brillouin zone of the primitive cells, where the k-path of Γ(0, 0, 0)–C(0.344, 0.344, 0)–Y_2(−0.5, 0.5, 0)–Γ(0, 0, 0)–M_2(−0.5, 0.5, 0.5)–D_2(0.313, 0.313, 0.5)–A(0, 0, 0.5)–Γ(0, 0, 0)–L_2(0, 0.5, 0.5)–Γ(0, 0, 0)–V_2(0, 0.5, 0) was considered for both systems.

Characterization

Powder X-ray diffraction (PXRD). The XRD patterns were collected using the powder diffractometer (STOE & Cie GmbH, Germany) in a mode of STOE STADI-MP, equipped with a Long Fine Focus C-Tech X-ray diffraction tube (Malvern Panalytical, Netherlands), with a Cu target (CuKα1 radiation = 1.5406 Å, Focus spot size 0.4 × 12 mm^2), a Germanium 111 crystal monochromator, and a Dectris Mythen2 R 1 K detector (Dectris AG, Switzerland).

Field emission scanning electron microscopy (FE-SEM). The elemental analysis of LDPNCs films was performed using FE-SEM JEOL-6700F in energy dispersive X-ray analysis (EDS) mode, operated with an accelerated electron beam to 20 kV with an in-lens detector.

Transmission electron microscopy (TEM). The TEM images and composition analysis were conducted using an environmental TEM (HF-3300S, Hitachi High-Technologies, Japan). This microscope is equipped with a cold-field emission gun and was operated at an acceleration voltage of 100 kV for all samples. The microscope is also equipped with an Oxford Instruments SDD X-MaxN 80 T detector to obtain XEDS spectra

Optical measurements. UV–Vis absorption spectra of LDPNCs either in solution (hexane) or in film state (on microscopy slide glass) were measured using a single-beam UV–Vis spectrometer (Thermo Scientific, Evolution 201). Steady-state photoluminescence (ss-PL) spectra were recorded by utilizing an Agilent Cary Eclipse Fluorescence Spectrophotometer featuring a xenon flash lamp (80 Hz, ~2 µs pulse width and dual Czerny-Turner monochromators covering 190–1100 nm for excitation and emission.

X-ray photoelectron spectroscopy (XPS). The XPS spectra were measured using non-monochromatized Mg Kα X-rays (hν = 1253.64 eV) that are generated by a twin anode X-ray source (RS 40B1, PREVAC) and a Phoibos 150 R7 analyzer (SPECS). The XPST package in Igor Pro was used to analyze all the XPS spectra.

Extended X-ray absorption spectroscopy (XAS). The XAS spectra were collected at the Balder beamline (MAX IV Laboratory synchrotron light facility, Lund University, Sweden)[60]. The first inflexion point of the Cu-foil (8979 eV) calibration was performed using a Pt-coated mirror with a liquid nitrogen-cooled double crystal (Si311) monochromator (FMB Oxford, UK). The initially focused X-ray beam, measuring 50 nm × 50 nm, was defocused to approximately 500 nm × 50 nm to enhance the signal-to-noise ratio. Ionization chambers (ICs) were employed to monitor the incident beam intensity (I_0), while a seven-element Ge detector, positioned at 90° to the beam path, was used to collect the fluorescence signal (I_f). The linear absorption coefficient, μ(E), is directly proportional to the ratio I_0/I_f. Data normalization and background subtraction were performed using the Larch Package[61], applying default parameters.

Temperature-dependent Fourier-transform infrared (FT-IR) spectroscopy. The FT-IR spectra of LDPNCs at a temperature range of 20–300 K were acquired using a Bruker IFS 125 HR FT-IR spectrometer equipped with a liquid nitrogen-cooled HgCdTe detector, a preamplifier, a KBr beamsplitter, and a helium gas flow cryostat. Thermoregulation was controlled via an ITC 503S controller, with a 5-min equilibration period following each temperature adjustment. Spectra were recorded with an instrument resolution of 2 cm^{-1}. Samples were prepared as pressed pellets mixed with KBR. Transmission spectra were derived by referencing to a sample of pure KBr.

Time-resolved photoluminescence (TRPL) measurements. The TRPL decays were measured using a Hamamatsu C6860 streak camera with the excitation from a Spectra-Physics Tsunami Ti:sapphire laser producing 60 fs pulses centered at 800 nm at a repetition rate of 80 MHz. Excitation pulses at 400 nm and 266 nm were generated by second-harmonic generation (SHG) and third-harmonic generation (THG), respectively, using a Tripler (TB-2000B). The system provided a temporal resolution of 20 ps with a slit width of 15 µm.

Ultrafast transient absorption spectroscopy (TAS). The TAS measurements for LDPNC films were performed using a custom-built femtosecond pump-probe setup. Solstice regenerative amplifier (Spectra Physics; 8 W, 796 nm, 60 fs, 4 kHz) is the laser source seeded by a Mai Tai SP femtosecond oscillator (Spectra Physics). The seedling laser is split into a pump beam (95% of full power) and a probe beam (5% of full power). Pump pulses at 400 nm (0.3–0.5 mW, 100 fs) were generated using a collinear optical parametric amplifier (TOPAS-C, light conversion) followed by second-harmonic generation (SHG) of the 800 nm fundamental pulses. Pump pulses at 266 nm (0.3–0.5 mW, 100 fs) were generated using a Tripler 100 M(X) (Spectra Physics), where the 400 nm s harmonic generated in a BBO crystal was mixed with 800 nm fundamental to produce the 266 nm sum-frequency input. Residual 400 and 800 nm components were removed using highly selective reflective mirrors. The excitation fluence was controlled using neutral density filters. The excitation intensities are changed in sequence by using the neutral density filter. For the probe, a broadband white-light continuum (480–900 nm, TA spectra measurement) was obtained by focusing the probe pulse onto a thin CaF_2 plate, where the 1350 nm pulse was generated by a collinear optical parameter amplifier (TOPAS-C Light Conversion). The probe beam is then split into two parts: one passes through the sample, and the other is sent directly to the detector for reference. To prevent photodamage to the samples, the sample position is changed after each scan.

Electrochemical measurements. Cyclic voltammogram (CV) of LDPNCs in suspension was measured using a three-electrode configuration connected to a potentiostat setup (PalmSens). The electrochemical cell consists of an Ag/AgCl stick as reference electrode (RE), a platinum disc as counter electrode (CE), and a platinum wire as working electrode (WE). The ferrocence/ferrocenium (Fc/Fc^+) as a redox couple was utilized as a standard of internal calibration. The energy level of the ferrocene calibration is set at −4.8 eV (Fc/Fc^+) vs. vacuum. To minimize oxygen interference during the reduction process, the prepared electrolyte solution was degassed by bubbling nitrogen gas for 10–15 min. The LDPNC-containing ≈0.15 mg/mL solution was prepared in DCM solvent that also contains 0.1 M $TBAPF_6$ as the electrolyte for a nonaqueous system with additional purging nitrogen for 10 min. CV scans were acquired at a scan rate of 0.01 V/s by monitoring the current response as a function of applied potential. The midpoint potential was used to calculate the valence and conduction band edge positions of the NCs according to the following equations[19,62]:

$$E_{VB} = -\left(E_{OX} - V\left(\frac{Fc}{Fc^+}\right) + 4.8\right) eV and E_{CB} = E_{VB} + E_g.$$

Moreover, electrochemical impedance spectroscopy (EIS) spectra of the LDPNCs film were measured using the same potentiostat (PalmSens) under both dark and light (1 Sun) conditions.

Data availability

The data that support the findings of this study are available from the corresponding author upon reasonable request.

Received: 20 June 2026; Accepted: 18 September 2026;
Published online: 07 October 2026

References

1. Chen, C. et al. Toxicity, leakage, and recycling of lead in perovskite photovoltaics. *Adv. Energy Mater.* **13**, 2204144 (2023).
2. Guan, X. et al. Targeted elimination of tetravalent-Sn-induced defects for enhanced efficiency and stability in lead-free NIR-II perovskite LEDs. *Nat. Commun.* **15**, 9913 (2024).
3. Liu, C. et al. $CsSnI_3$ quantum dots as a multifunctional interlayer for high-efficiency bilayer perovskite solar cells. *Adv. Energy Mater.* **15**, 2405074 (2025).
4. Li, N. et al. ZnSe Nanorods–$CsSnCl_3$ Perovskite heterojunction composite for photocatalytic CO_2 reduction. *ACS Nano* **16**, 3332–3340 (2022).
5. Liang, W. et al. Efficient optical orientation and slow spin relaxation in lead-free $CsSnBr_3$ perovskite nanocrystals. *ACS Energy Lett.* **6**, 1670–1676 (2021).
6. Jellicoe, T. C. et al. Synthesis and optical properties of lead-free cesium tin halide perovskite nanocrystals. *J. Am. Chem. Soc.* **138**, 2941–2944 (2016).
7. Zhang, X. et al. Trade-off between toxicity and efficiency in tin- versus lead-based halide perovskites. *Angew. Chem. Int. Ed.* **64**, e202500557 (2025).
8. Qiu, X. et al. From unstable $CsSnI_3$ to air-stable Cs_2SnI_6: a lead-free perovskite solar cell light absorber with bandgap of 1.48 eV and high absorption coefficient. *Sol. Energy Mater. Sol. Cells* **159**, 227–234 (2017).
9. Wang, J. et al. Enabling enhanced photocatalytic hydrogen evolution in water by doping Cs_2SnBr_6 perovskite with Pt. *ACS Energy Lett.* **9**, 653–661 (2024).
10. Maughan, A. E. et al. Defect tolerance to intolerance in the vacancy-ordered double perovskite semiconductors Cs_2SnI_6 and Cs_2TeI_6. *J. Am. Chem. Soc.* **138**, 8464 (2016).
11. Umedov, S. T. et al. A-site tailoring in the vacancy-ordered double perovskite semiconductor Cs_2SnI_6 for photovoltaic application. *Sol. Energy Mater. Sol. Cells* **230**, 111180 (2021).
12. Zhou, P. et al. Single-atom Pt-I_3 sites on all-inorganic Cs_2SnI_6 perovskite for efficient photocatalytic hydrogen production. *Nat. Commun.* **12**, 4412 (2021).
13. Vargas, B. et al. A direct bandgap copper–antimony halide perovskite. *J. Am. Chem. Soc.* **139**, 9116–9119 (2017).
14. Vargas, B. et al. Chemical diversity in lead-free, layered double perovskites: A combined experimental and computational approach. *Chem. Mater.* **32**, 424–429 (2020).
15. Cai, T. et al. Lead-Free $Cs_4CuSb_2Cl_{12}$ layered double perovskite nanocrystals. *J. Am. Chem. Soc.* **142**, 11927–11936 (2020).
16. Mai, H. et al. Synthesis of layered lead-free perovskite nanocrystals with precise size and shape control and their photocatalytic activity. *J. Am. Chem. Soc.* **145**, 17337–17350 (2023).
17. Liu, M. et al. Moisture-assisted near-UV emission enhancement of lead-free $Cs_4CuIn_2Cl_{12}$ double perovskite nanocrystals. *Nano Lett.* **22**, 311–318 (2022).
18. Liu, M. et al. Lattice engineering via transition metal ions for boosting photoluminescence quantum yields of lead-free layered double perovskite nanocrystals. *Small* **20**, 202401051 (2024).
19. Yukta et al. M(III) site-driven structural engineering on lead-free layered double perovskite nanocrystals with enhanced photoelectrochemical activity. *Small Struct.* **6**, 202500179 (2025).
20. Wang, X. D. et al. The top-down synthesis of single-layered $Cs_4CuSb_2Cl_{12}$ halide perovskite nanocrystals for photoelectrochemical application. *Nanoscale* **11**, 5180–5187 (2019).
21. Liu, Z. et al. Design of mixed-cation tri-layered pb-free halide perovskites for optoelectronic applications. *Adv. Electron. Mater.* **5**, 1900234 (2019).
22. Kelton, K. F. Crystal nucleation in liquids and glasses. *Solid State Phys.* **45**, 75–177 (1991).
23. Shannon, R. D. Revised effective ionic radii and systematic studies of interatomic distances in halides and chalcogenides. *Acta Crystallogr. Sect. A.* **32**, 751–767 (1976).
24. Pal, J. et al. Colloidal synthesis and photophysics of $M_3Sb_2I_9$ (M=Cs and Rb) Nanocrystals: lead-free perovskites. *Angew. Chem. Int. Ed.* **56**, 14187–14191 (2017).
25. Hewitt, R. W. & Winograd, N. Oxidation of polycrystalline indium studied by x-ray photoelectron spectroscopy and static secondary ion mass spectroscopy. *J. Appl. Phys.* **51**, 2620–2624 (1980).
26. Faur, M. et al. XPS investigation of anodic oxides grown on p-type InP. *Surf. Interface Anal.* **15**, 641–650 (1990).

27. Kudo, Y. et al. Acid-dissociation behavior of para-hydroxyl group in the N,N,O-Terdentate Ligand, 4-(4-Methyl-2-pyridylazo) resorcinol, coordinated to a transition metal ion. *Bull. Chem. Soc. Jpn.* **59**, 1481–1486 (1986).
28. Hu, M. et al. Photovoltaics of low-bandgap inorganic perovskites. *Green. Carbon* **2**, 263–273 (2024).
29. Süzer, Ş et al. Electron spectroscopic investigation of Sn coatings on glasses. *Fresenius J. Anal. Chem.* **355**, 654–656 (1996).
30. Okamoto, Y. et al. A study of the interaction of Pb-Sn Solder with O_2, H_2O, and NO_2 by X-Ray Photoelectron (ESCA) and Auger (AES) Spectroscopy. *Appl. Spectrosc.* **33**, 287–293 (1979).
31. Grutsch, P. A. et al. Photoelectron spectroscopy of tin compounds. *Inorg. Chem.* **12**, 1431–1433 (1973).
32. Lin, A. W. C. et al. X-ray photoelectron/auger electron spectroscopic studies of tin and indium metal foils and oxides. *Anal. Chem.* **49**, 1228–1235 (1977).
33. Wang, J. et al. An investigation of the flame retardation mechanism of polypropylene containing a chlorine flame retardant system by XPS(ESCA). *Polym. Degrad. Stab.* **31**, 129–140 (1991).
34. Kang, D. H. et al. Extended X-ray absorption fine structure (EXAFS) of $FAPbI_3$ for understanding local structure-stability relation in perovskite solar cells. *J. Energy Chem.* **67**, 549–554 (2022).
35. Welyab, G. et al. All-inorganic $CsPbBr_3$ perovskite nanocrystals synthesized with olive oil and oleylamine at room temperature. *Micromachines* **14**, 1332 (2023).
36. Ji, Y. et al. DFT-Calculated IR spectrum amide I, II, and III band contributions of N-methylacetamide fine components. *ACS Omega* **5**, 8572–8578 (2020).
37. Kühne, T. D. et al. CP2K: an electronic structure and molecular dynamics software package -Quickstep: efficient and accurate electronic structure calculations. *J. Chem. Phys.* **152**, 194103 (2020).
38. Perdew, J. P. et al. Generalized gradient approximation made simple. *Phys. Rev. Lett.* **77**, 3865 (1996).
39. Runge, E. & Gross, E. K. U. Density-functional theory for time-dependent systems. *Phys. Rev. Lett.* **52**, 997 (1984).
40. Yang, B. & Han, K. Ultrafast dynamics of self-trapped excitons in lead-free perovskite nanocrystals. *J. Phys. Chem. Lett.* **12**, 8256–8262 (2021).
41. Swarnkar, A. et al. Beyond colloidal cesium lead halide perovskite nanocrystals: analogous metal halides and doping. *ACS Energy Lett.* **2**, 1089–1098 (2017).
42. Yuan, Y. et al. Shallow defects and variable photoluminescence decay times up to 280 μs in triple-cation perovskites. *Nat. Mater.* **23**, 391–397 (2024).
43. Maduwanthi, C. et al. Charge carrier dynamics controlling performance of lead-based halide perovskite solar cells. *Jpn. J. Appl. Phys.* **64**, 050806 (2025).
44. Pasanen, H. P. et al. Fast non-ambipolar diffusion of charge carriers and the impact of traps and hot carriers on it in CsMAFA perovskite and GaAs. *Mater. Adv.* **2**, 6613–6619 (2021).
45. Makuta, S. et al. Photo-excitation intensity dependent electron and hole injections from lead iodide perovskite to nanocrystalline TiO_2 and spiro-OMeTAD. *Chem. Commun.* **52**, 673–676 (2015).
46. Lam, L. K. M. et al. Reduction of benzoquinones to hydroquinones via spontaneous reaction with glutathione and enzymatic reaction by S-glutathionyl-hydroquinone reductases. *Biochemistry* **51**, 5014–5021 (2012).
47. Yang, M. Z. et al. Constructing $CsPbBr_xI_{3-x}$ nanocrystal/carbon nanotube composites with improved charge transfer and light harvesting for enhanced photoelectrochemical activity. *J. Mater. Chem. A Mater.* **7**, 5409–5415 (2019).
48. Liu, M. et al. Water-resistant perovskite-inspired copper/silver pnictohalide nanocrystals for photoelectrochemical water splitting. *Electrochim. Acta* **462**, 142734 (2023).
49. Liu, M. et al. Influence of hole mobility on charge separation and recombination dynamics at lead halide perovskite and spiro-OMeTAD interface. *J. Photopolym. Sci. Technol.* **32**, 727–733 (2019).
50. Lazanas, A. C. & Prodromidis, M. I. Electrochemical Impedance spectroscopy: a tutorial. *ACS Meas. Sci. Au* **2023**, 162–193 (2023).
51. Kresse, G. & Hafner, J. Ab initio molecular dynamics for liquid metals. *Phys. Rev. B.* **47**, 558 (1993).
52. Kresse, G. & Furthmüller, J. Efficiency of ab-initio total energy calculations for metals and semiconductors using a plane-wave basis set. *Comput. Mater. Sci.* **6**, 15–50 (1996).
53. Kresse, G. & Furthmüller, J. Efficient iterative schemes for ab initio total-energy calculations using a plane-wave basis set. *Phys. Rev. B.* **54**, 11169 (1996).
54. Kresse, G. & Joubert, D. From ultrasoft pseudopotentials to the projector augmented-wave method. *Phys. Rev. B* **59**, 1758 (1999).
55. Blöchl, P. E. Projector augmented-wave method. *Phys. Rev. B.* **50**, 17953 (1994).
56. Åtich, I. et al. Conjugate gradient minimization of the energy functional: A new method for electronic structure calculation. *Phys. Rev. B.* **39**, 4997 (1989).
57. Adamo, C. & Barone, V. Toward reliable density functional methods without adjustable parameters: the PBE0 model. *J. Chem. Phys.* **110**, 6158–6170 (1999).
58. Perdew, J. P. et al. Density-functional theory for fractional particle number: derivative discontinuities of the Energy. *Phys. Rev. Lett.* **49**, 1691 (1982).
59. Blöchl, P. E. et al. Improved tetrahedron method for Brillouin-zone integrations. *Phys. Rev. B.* **49**, 16223 (1994).
60. Klementiev, K. et al. The BALDER Beamline at the MAX IV Laboratory. *J. Phys. Conf. Ser.* **712**, 012023 (2016).
61. Newville, M. Larch: An analysis package for XAFS and related spectroscopies. *J. Phys. Conf. Ser.* **430**, 012007 (2013).
62. Liu, M. et al. Manganese doping promotes the synthesis of bismuth-based perovskite nanocrystals while tuning their band structures. *Small* **17**, e2100101 (2021).

Acknowledgements

M.L., S.R., Yukta, T.H., V.S. and Q.Z. acknowledges Crafoord Foundation (No. 20240745), Swedish Research Council (decision No. 2025-05257 and 2025-08113), NanoLund (project No. p04-2025), Royal Physiographic Society of Lund, LU Profile Area of Light & Materials, and LU Sustainability Fund for funding. This work was partially supported by the Wallenberg Initiative Materials Science for Sustainability (WISE), funded by the Knut and Alice Wallenberg Foundation. A.N. and J.W. acknowledge funding from the Swedish Strategic Research Foundation through a Future Research Leader programme (FFL21-0129), the European Research Council (ERC Starting Grant No. 101162195), and the Knut and Alice Wallenberg Foundation (Nos. 2023.0032 and 2024.0042). The computations were enabled by resources provided by the National Academic Infrastructure for Supercomputing in Sweden (NAISS) at C3SE, PDC, and NSC, partially funded by the Swedish Research Council through grant agreement No. 2022-06725. T.P. and Q.S. acknowledge financial support from Olle Engqvists foundation (235-0422), Swedish Foundation for Strategic Research (SSF, IS24-0005), and LU Profile Area of Light & Materials. The authors acknowledge the MAX IV Laboratory for beamtime on the FinEstBeAMS beamline under proposal (proposal ID: 20252221). Research conducted at MAX IV, a Swedish national user facility, is supported by Vetenskapsrådet (Swedish Research Council, VR) under contract 2018-07152, Vinnova (Swedish Governmental Agency for Innovation Systems) under contract 2018-04969 and Formas under contract 2019-02496. The authors also thank Dr. Justus Just for the XAS measurements (proposal ID:20241032) at the BALDER beamline, MAX IV Laboratory, Lund, Sweden. The Energy Materials In-situ Laboratory (EMIL) operated by Helmholtz-Zentrum Berlin is thanked for granting access to its chemistry laboratory.

Author contributions

S.R.: Methodology; Data curation; Formal analysis; Validation; Investigation; Writing—original draft. A.N.: Data curation; Formal analysis; Software; Validation; Writing—review & editing. Yukta: Data curation; Formal analysis; Investigation; Writing—review & editing. Q.S.: Data curation; Formal analysis; Writing—review & editing. T.H.: Data curation; Formal analysis; Writing—review & editing. V.S.: Formal analysis; Validation; Writing—review & editing. S.B.: Data curation; Formal analysis. K.P.: Data curation; Formal analysis. T.A.S.: Data curation; Formal analysis; Writing—review & editing. S.K.M.: Data curation; Software; Investigation. Q.Z.: Data curation; Formal analysis; Visualization; Writing—review & editing. J.L.: Data curation; Formal analysis. W.W.: Data curation: Formal analysis; Resources; Writing—review & editing. K.A.D.: Resources; Supervision; Funding acquisition. T.P.: Formal analysis; Resources; Supervision; Writing—review & editing; Funding acquisition. M.L.: Conceptualization; Methodology; Validation; Formal analysis; Resources; Writing—original draft; Supervision; Projection administration; Funding acquisition.

Funding

Open access funding provided by Lund University.

Competing interests

The authors declare no competing interests.

Additional information

Supplementary information The online version contains supplementary material available at https://doi.org/10.1038/s43246-026-01388-3.

Correspondence and requests for materials should be addressed to Maning Liu.

Peer review information *Communications Materials* thanks the anonymous reviewers for their contribution to the peer review of this work.

Reprints and permissions information is available at http://www.nature.com/reprints

Publisher's note Springer Nature remains neutral with regard to jurisdictional claims in published maps and institutional affiliations.

Open Access This article is licensed under a Creative Commons Attribution 4.0 International License, which permits use, sharing, adaptation, distribution and reproduction in any medium or format, as long as you give appropriate credit to the original author(s) and the source, provide a link to the Creative Commons licence, and indicate if changes were made. The images or other third party material in this article are included in the article's Creative Commons licence, unless indicated otherwise in a credit line to the material. If material is not included in the article's Creative Commons licence and your intended use is not permitted by statutory regulation or exceeds the permitted use, you will need to obtain permission directly from the copyright holder. To view a copy of this licence, visit http://creativecommons.org/licenses/by/4.0/.

© The Author(s) 2026